PAPER

Check for updates

Heterotypic tumor models through freeform printing into photostabilized granular microgels†

Thomas G. Molley, [ID] [a] Gagan K. Jalandhra,[a] Stephanie R. Nemec,[a] Aleczandria S. Tiffany,[b] Amrutha Patkunarajah,[e] Kate Poole, [ID] [e] Brendan A. C. Harley, [ID] [b,c,d] Tzong-tyng Hung[f] and Kristopher A. Kilian [ID] *[a,g]

The tissue microenvironment contains a complex assortment of multiple cell types, matrices, and vessel structures, which is difficult to reconstruct *in vitro*. Here, we demonstrate model tumor microenvironments formed through direct writing of vasculature channels and tumor cell aggregates, within a cell-laden microgel matrix. Photocrosslinkable microgels provide control over local and global mechanics, while enabling the integration of virtually any cell type. Direct writing of a Pluronic sacrificial ink into a stromal cell-microgel suspension is used to form vessel structures for endothelialization, followed by printing of melanoma aggregates. Tumor cells migrate into the prototype vessels as a function of spatial location, thereby providing a measure of invasive potential. The integration of perfusable channels with multiple spatially defined cell types provides new avenues for modelling development and disease, with scope for both fundamental research and drug development efforts.

1 Introduction

Tumor progression and dissemination are influenced through local microenvironment mechanics and degradability,[1] surface topology,[2,3] and paracrine and autocrine signaling between tumor cells and surrounding stroma.[4–6] Within this complex microenvironment, blood and lymphatic vessels play critical roles in feeding the primary tumor, while also providing an avenue for dissemination through intravasation and extravasation.[7] While simple co-culture models from transwell plates,[8] monolayers,[9] 3-dimensional (3D) spheroid co-cultures,[10] and cell-embedded hydrogel matrices[11] have yielded great insights into tumor-stroma and vasculature interactions, considerable

work remains to realize full spatiotemporal control in 3D—an essential task for understanding the functional relationships of cells, stroma, and molecular interactions in this multivariate space. And given the complexity of the signaling underlying tumor progression, creation of robust models that assemble multiple cell types *in vitro* has remained a challenge.[12]

3D bioprinting has emerged as a promising tool to attenuate the spatiotemporal properties of cells and their surrounding matrices to build better tissue models for fundamental research and drug development. Recently, printing into support baths of suspended microgels has garnered considerable attention as a route to fabricating complex tissue mimics.[13–19] These support baths fluidize under shear force as the microgel particles near the print nozzle translate around the tip, while subsequently supporting the ink that is deposited. This enables the freeform printing of inks in all dimensions, allowing for complex structures and taller prints.[20] Concurrently, Lewis and colleagues created the first method for directly writing vasculature through sacrificial inks to create vascularized hydrogels[21,22] and they have further extended this work to printing into a support bath of organoids to form thick vascularized tissues.[23,24] These approaches have demonstrated the versatility of printing in granular media, and the potential to fabricate defined vessel structures.

Here, we present freeform vascular printing in cell-laden microgel suspensions where a sacrificial ink deposited within photocrosslinkable microgels defines hollow channels amidst printed cancer and stromal structures. The platforms modularity enables virtually any combination of cells to be spatially

[a]School of Materials Science and Engineering, University of New South Wales, Sydney, NSW 2052, Australia. E-mail: k.kilian@unsw.edu.au
[b]Department of Chemical and Biomolecular Engineering, University of Illinois at Urbana-Champaign, Urbana, IL 61801, USA
[c]Cancer Center at Illinois, University of Illinois at Urbana-Champaign, Urbana, IL 61801, USA
[d]Carl R. Woese Institute for Genomic Biology, University of Illinois at Urbana-Champaign, Urbana, IL 61801, USA
[e]EMBL Australia Node in Single Molecule Science, School of Medical Sciences, Faculty of Medicine & Health, University of New South Wales, Sydney, NSW 2052, Australia
[f]Biological Resources Imaging Laboratory, Mark Wainwright Analytical Centre, University of New South Wales, Sydney, NSW 2052, Australia
[g]School of Chemistry, Australian Centre for Nanomedicine, University of New South Wales, Sydney, NSW 2052, Australia
†Electronic supplementary information (ESI) available. See DOI: 10.1039/d1bm00574j

defined within controlled proximity to prototype vascular channels. As proof of principle of our systems versatility, we demonstrate the granular gels capacity to model tumor progression by spatially organizing three important contributors: (1) stromal cells dispersed uniformly within the microgel suspension, (2) primary tumor cells and structures in defined 3D architectures, and (3) endothelial cells within interpenetrating hollow channels (Fig. 1A). Further microenvironment control is afforded by changing the microgel composition and chemistry, facilitating tunable local and global mechanics of the microgel construct.

2 Results

2.1 Creating photocrosslinkable support gels

In contrast to dissolvable gelatin microparticles used in previous work,[15,16] we synthesized gelatin–methacryloyl (GelMa) microparticles using a water-in-oil emulsion; liquid GelMa is added dropwise to 40 °C oil under stirring followed by cooling to 10 °C to physically crosslink the microparticles, leaving methacryloyl moieties for further crosslinking. Adding acetone then dehydrates the microparticles and allows for easy washing and weighing. When rehydrated, the microparticles have an approximate diameter of 100 microns (Fig. 2A). Since yield stress fluid properties can vary greatly with small changes in suspension compositions, we weighed and hydrated our dried microparticles with consistent particle to liquid ratios. These suspensions were rested for at least 24 hours prior to use since acetone dried GelMa can take days to rehydrate (Fig. S1†). At hydrated volume fractions of ~50–65%, the microparticles reach a jammed state where they lock in place by frictional and repulsion forces.[20] These jammed particle suspensions behave as a solid under equilibrium conditions but will flow like a liquid once a critical shear force is applied. Swelling tests of the GelMa microparticles showed they rehydrate to ~10× their dried weight, which we used to hydrate our suspensions to the target 60% volume fraction of particles consistently.

By functionalizing the gelatin with methacryloyl groups, our microparticle suspensions can be chemically crosslinked within and between the particles to stabilize the matrix. After exposure to 60 seconds of 395 nm light on a rheometer, the microgels gain a 2 order of magnitude increase in storage modulus (Fig. 2B) and become stable under shear forces (Fig. S2A†). To gain greater control of the local mechanics of the gel as well as aid in printability, we added a fraction of soluble GelMa to provide a means of effectively "stitching" the jammed suspension together after printing. By hydrating the dried particles with a liquid solution of low weight percent GelMa, the same bulk rheological properties of the microgel suspension can be maintained, while now creating a soft matrix around the stiff particles. When hydrating the particles to 40% volume fraction with a 1 wt% GelMa solution as the liquid filler, we achieve near identical bulk mechanical properties to the jammed microparticles (no filler) while changing the interstitial space from pure liquid to a soft matrix (Fig. 2B). When applying a shear strain rate sweep on the suspensions, both exhibit similar yield stress fluid properties—each demonstrating high printability. Suspension with fillers also demonstrate stability under shear forces once photocrosslinked (Fig. S2A†). Decreasing the light exposure had minimal effect on the gel strength of filler suspensions with a <1% decrease in storage modulus; however, increasing light exposure to 120 seconds gave a 23% increase (Fig. S2B†). Stabilized suspen-
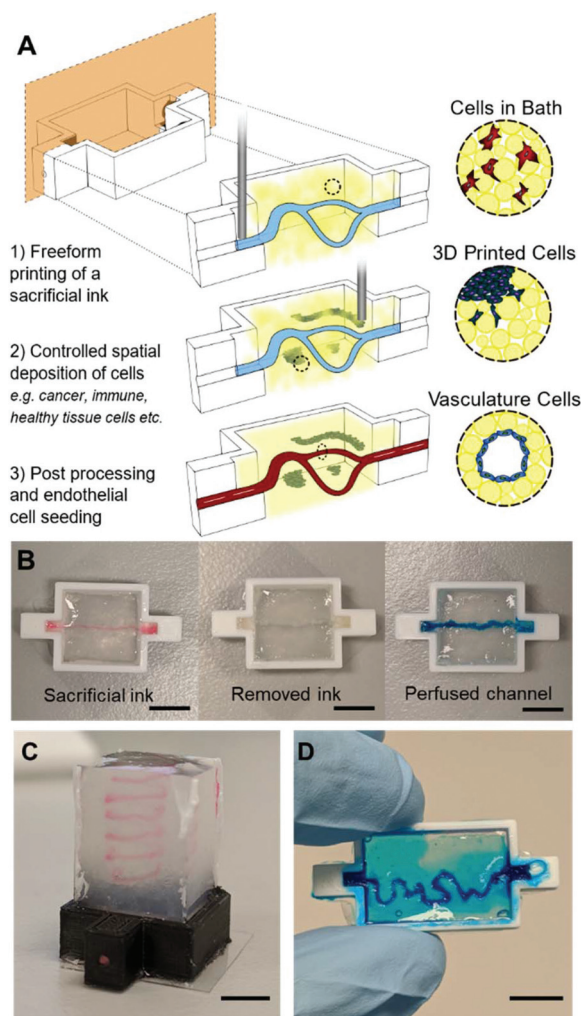

Fig. 1 Photocrosslinking to stabilize suspension microgels allows for complex organization of cells in three distinct ways. (A) (1) An uncrosslinked microgel suspension, with or without cells, is placed in a reactor where a sacrificial ink is freeformly printed. (2) More cell types can further be printed as different shapes and sizes at various proximities to the sacrificial ink. (3) The suspension is photocrosslinked followed by removal of the sacrificial ink and subsequent seeding of endothelial cells on the hollow channel walls. (B) Macro images of the three stages of hollow channel formation: printing of the ink, photocrosslink and evacuation of the ink, and perfusion of the hollow channel for seeding. (C) A macro image of a 7 mm tall spiral print of Pluronic F127 ink in microgel suspension. (D) An image of blue dye that has been perfused through the letters "UNSW" that were printed and evacuated. Scale bars: 5 mm (B, C and D).
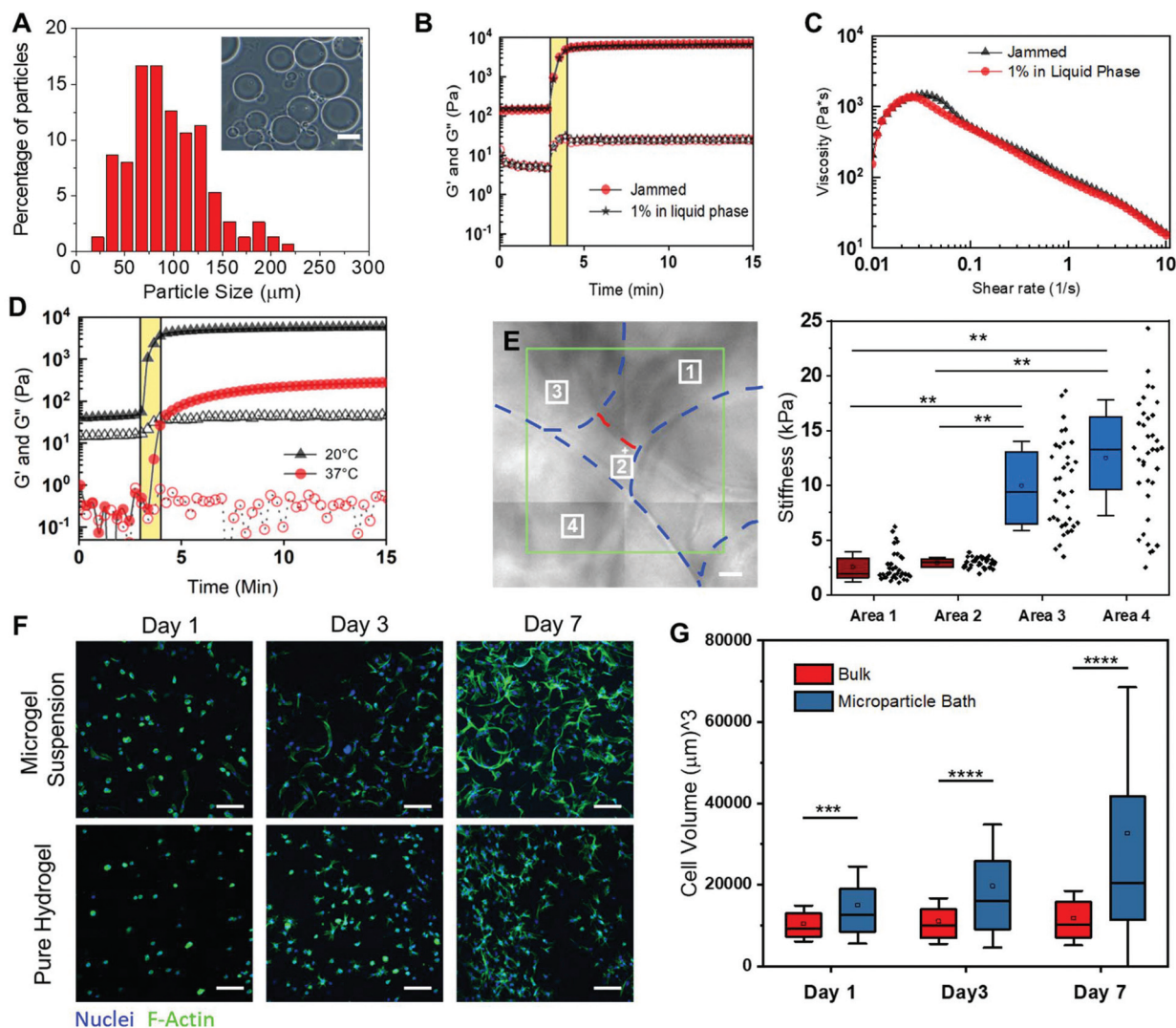
Fig. 2 Characterization of GelMa microparticle support suspensions for 3D printing. (A) Size distribution (n = 100) of the 10 wt% GelMa microparticles. Inset image is a representative optical image of the microparticles. (B) Rheological analysis of the gelation of suspensions with (red markers) and without (black markers) a 1 wt% GelMa filler in the liquid phase. Closed markers are the storage modulus (G') and open markers are the loss modulus (G'') The yellow bar indicates UV crosslinking. (C) Uncrosslinked microgel viscosity as a function of Shear rate for suspensions with (red markers) and without (black markers) filler. (D) Effect of melting a microgel suspension (red markers) on the storage modulus (G') when compared to unmelted heterogenous suspension (black markers). The yellow bar indicates UV crosslinking. (E) Contact mode atomic force microscopy (AFM) over 4 regions of a suspension bath surface. Force curves (n = 36 per square, p < 0.001) were taken at each 10 μm × 10 μm region of the surface where the analyzed young's modulus is plotted for each region's curves. (F) Z-stack projections (100 μm z-stacks of 50 slices) of ADSCs stained with Hoechst (blue) and Phalloidin (green) in microgel suspensions and a pure hydrogel (10 wt% GelMa). (G) Box plots of cell volume quantification of microgel suspensions *vs.* pure hydrogels over 7 days (*** = p < 0.001, ** = p < 0.0001). Scale bars: 10 μm (E), 100 μm (F).

sions warmed to 37 °C where the physical crosslinks release had a drop in strength of only 7% (Fig. S2C†), demonstrating stability of the network through the covalent modifications. The bulk mechanical properties can also be tuned by varying the weight percentage of the GelMa used to make the microgel suspension, where particles formed with 15 wt% GelMa formed suspensions with a 70% higher storage modulus (Fig. S3†).

It is well appreciated that both global and local mechanical environments can play a large role in directing cell function and behavior.[25,26] Therefore, multiple classes of mechanical

testing are required for this type of heterogeneous microgel suspension. To highlight this heterogeneity, we melted a suspension solution prior to photocrosslinking and found a decrease in strength of nearly two orders of magnitude (Fig. 2D). We further demonstrate this heterogeneity with AFM force curves (1 μm radius spherical borosilicate probe, 36 curves per 10 μm × 10 μm regions) taken at 4 different locations across the surface of our crosslinked microgel. The regions over the microparticles have relative moduli of over 5 times that of the filler regions (Fig. 2E). However, even over the stiffer particles, there is wide variation at the local scale as the

filler material wraps itself not only between particles, but around them as well, creating broad variability in stiffness the cell experiences. This contrasts with similar microporous particle scaffold (MAP) systems that contain discrete pockets of heterogeneity.[20]

We next set out to explore the exciting possibility that our printing support matrix would be beneficial to integrated live cells. We began by seeding adipose derived stem cells (ADSCs) at one million cells per ml of microgel suspension. Initial live/dead staining of cells indicated high cell viability (Fig. S4†). However, the nature of the scaffolds made it difficult to image samples thicker than 0.5 mm. The particles have a much higher index of refraction compared to the filler phase, thus leading to significant light scattering during imaging. To circumvent this limitation, we adapted our recently reported optical clearing technique[27,28] where index matching allows increased imaging depth with minimal light scattering (Fig. S5†). To evaluate our clearing and imaging protocol, we loaded one million ADSCs per ml into our suspension, with a pure bulk GelMa matrix of comparable mechanics as a comparison. Given the porous nature of the microgels, and the tendency for cells to spread anisotropically in 3D, we sought to compare cell volume and surface area in 3D rather than with 2D projections. High resolution z-stacks of cells stained with phalloidin and Dapi were imported into Imaris to segment the cell and nuclear volumes (Fig. S6A†). There are increasingly significant differences of cell volume between our suspension and bulk GelMa on days 1, 3 and 7 (day 1 $p < 0.001$; day 3, 7 $p = 0.0001$) with the suspension cells increasing volume by ~100% from day 1 to 7 ($p = 0.001$) (Fig. 2G). A homogenous bulk GelMa matrix of comparable stiffness is dense and constricting to embedded cells, causing them to adopt a stellate morphology as they extend protrusive features and attempt to degrade the surrounding matrix. While no significant difference in cell volume was found across any days for the bulk gels, cell surface area measurements show a ~25% increase from day 1 to 3 ($p = 0.024$) and a ~50% increase from day 1 to 7 ($P = 0.001$) (Fig. S6B†). Cell sphericity measurements also indicate decreasing sphericity as volume and surface area increase, as well as less sphericity of cells embedded in the microgel matrix (Fig. S6C†). Over time, the cells within the microgels proliferated and adopted enhanced spreading on the microsphere architectures, suggesting both viability and bioactivity in the interconnected network.

2.2 Printing a sacrificial ink to create vasculature

To vascularize our gels, we designed and 3D printed plastic (Poly lactic acid (PLA)) molds with inlets for aligning needles for removal of the sacrificial ink and the seeding of vascular cells (Fig. S7A†). Since our scaffolds melt at physiological temperatures, we needed a sacrificial ink that liquifies as its temperature is lowered. Pluronic F127 was chosen as Lewis and colleagues have shown great success using this material in direct writing due to the tunable lower critical temperature.[22,29,30] Initially, we found that if the Pluronic F127

was not fully solidified, it would swell with water as printed, begin diffusing apart, and not anchor as it was printed. Therefore, we used 29 wt% Pluronic F127 for defining our vasculature channels because it fully sets at our laboratory's ambient temperature (19 °C) (Fig. S7B–D†). Red and blue dyes were added to the Pluronic ink to aid with visualization. Troughs were added to our vascular printing reactors to facilitate ink removal and cell seeding (Fig. 3A). After ink deposition, the suspension is photo crosslinked and the microgel is placed in the refrigerator (4 °C) for 10–15 minutes to liquify the Pluronic F127. The ink is then removed by syringe, leaving a hollow channel inside the microgel matrix (Fig. S7E†).

To create a system where consistent printing and reproducibility is ensured, we optimized printing parameters through design of experiments using print speed, print acceleration, extrusion volume multipliers, print height from reactor base, and suspension viscosity (data not shown). To aid with replication and advancement of our system, all GCODE used for printing has been hosted on a public GitHub repository (https://github.com/tmolley2/Vascular-printing.git). For all vascular printing, a 0.41 µm diameter syringe tip was used (22G Nordson EFD tip) given it is within the standard range for mimetic vasculature literature.[31,32] During optimization, we noticed that when the Pluronic was printed at a rate of 5 mm s^{-1} or higher, the ink tended to over-extrude causing the print to break apart (Fig. 3B). Since our setup uses a screw-based extruder over conventional pneumatic print heads for bioprinting, the printer should theoretically print the same volume of ink per distance under any given speed. However, Pluronic is a viscoelastic ink which can cause it to undergo die swell at the high shear forces applied at the fast print speeds of 5 mm s^{-1} and above. We found that 2.5 mm s^{-1} gave the most consistent channel width when printing, giving only a 7.5 ± 8% difference in diameter across the channel, so we proceeded with this extrusion rate for our vasculature printing in the majority of studies. However, when printing high curvature regions, such as those depicted in Fig. 1D, a speed of only 0.33 mm s^{-1} was best for maintaining overall print shape and was used for the UNSW logo (Fig. 1D). More printing guidelines can be found in the ESI.† By printing the ink back over itself, separately printed channels can be joined to create hierarchical architectures (Fig. 3C) (ESI Video 1†). Finally, to establish the broad potential for freeform vascular printing of complex paths, we printed a large perfusable spiral construct in a 5 mL suspension (Fig. 3D) (ESI Video 2†). This optimization of the ideal speeds and printing conditions of the sacrificial ink enables us to finely tune the quality and fidelity of the vasculature with the goal of creating more accurate vascular models.

Given that printing resolution is inherently limited by the size of microparticles in a suspension,[16] we wanted to verify that our channels maintained similar topology and wall stress along their entire length. We additionally wanted to verify if the flow characteristics were comparable to native blood vessels. To accomplish this, we performed MicroCT on printed
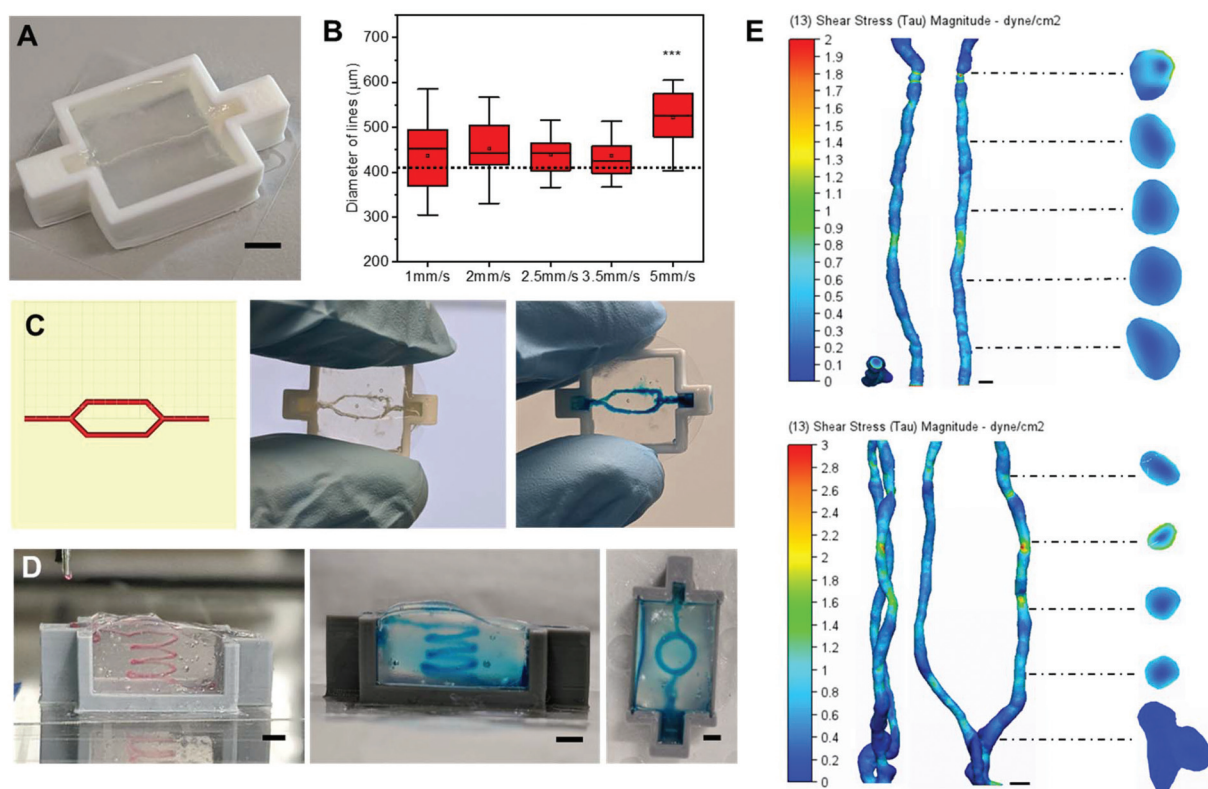
Fig. 3 Freeform printing of complex perfusable channels. (A) An image of a hollow channel in the Poly lactic acid (PLA) 3D printed reactors used for vascular printing. (B) Box plots of diameters of the Pluronic F127 ink (n = 28–35) printed into suspension baths at different speeds (5 mm s^{-1} compared to 1,2, 2.5, & 3.5 mm s^{-1}; p = 0.0101). (C) Images of the print head tool path for a bifurcation in Pronterface (left) followed by an evacuated bifurcation print (center) and the same print perfused with a blue dye (right). (D) Images of a four-loop spiral printed with Pluronic F127 (right) that was evacuated and perfused with a blue dye (center and right). (E) Wall shear stress heat maps for computation fluid dynamics (CFD) simulations run on representative single (top) and bifurcated (bottom) channels imaged *via* MicroCT. Scale bars: 3 mm (A and D), 400 μm (E).

single and bifurcated channels to create a 3D model of the void space. The microgel's high protein and water content allowed us to segment the microgel volume against air in the channel rather than using contrasting agents (Fig. S8A and S9A†). Computational fluid dynamics (CFD) analysis was performed on the segmented channel volumes to measure wall shear stress along the channel lengths under theoretical flow (150 nL per second for straight channel, and 300 nL per second for the bifurcation) (Fig. 3E). The variation of shear stress along the channel varies by ~100% while also achieving a similar stress level within 12% to the theoretical/ideal channel design (0.72 dyn cm^{-2} for ideal, 0.64 dyn cm^{-2} for the printed channel). Given that blood vessels experience a stress range from 3–30 dyn cm^{-2}, we find this variation to be acceptable.[32] Fluid flow vectors also show the fluid path in both channel types (Fig. S8B and S9B†) with little deviation from the ideal channel conditions. Laminar flow is seen without the presence of eddies in both channel types, with similar flow patterns between the experimental and the theoretical channel designs (ESI Videos 3–6†). And a plot of the average flow velocity magnitudes for ideal *vs.* printed channels gives only a ~25% variation. Taken together, these data indicate adequate flow characteristics.

2.3 Forming endothelial linings and printing cancer cells

Having established a method to fabricate hollow channels within the microgels, we next investigated the ability to integrate prototype vascular cells. Human umbilical vascular endothelial cells (HUVECs) were injected into the channels (10^7 cells per mL) to create vascular linings. The gels were rotated every 30 minutes for 1 hour to allow the cells to attach to the luminal surface on both sides. After 5 days of culture the HUVECs were seen to adhere and proliferate to the undulating topology of the channel with clear vessel linings at the luminal surface (Fig. 4A and B). While some gaps remain in regions between microparticles making the linings incomplete (Fig. 4C), we sought to test their impact on the barrier function of our endothelial lining. A solution of fluorescent dextran molecules (100 μg mL^{-1}, 40 kDa, FITC) was added to the channel of cell-free gels as well as endothelialized gels (4 days of culture post seeding). Images were taken on an epifluorescence microscope at 5-minute intervals. Line intensity profiles for each time point were fitted to a Gaussian curve and plotted to calculate the diffusion coefficient (Fig. S12†). The cell lined channels had a 3.5-fold reduction of diffusional permeability when compared to the cell-free (bare) channels. Tests were
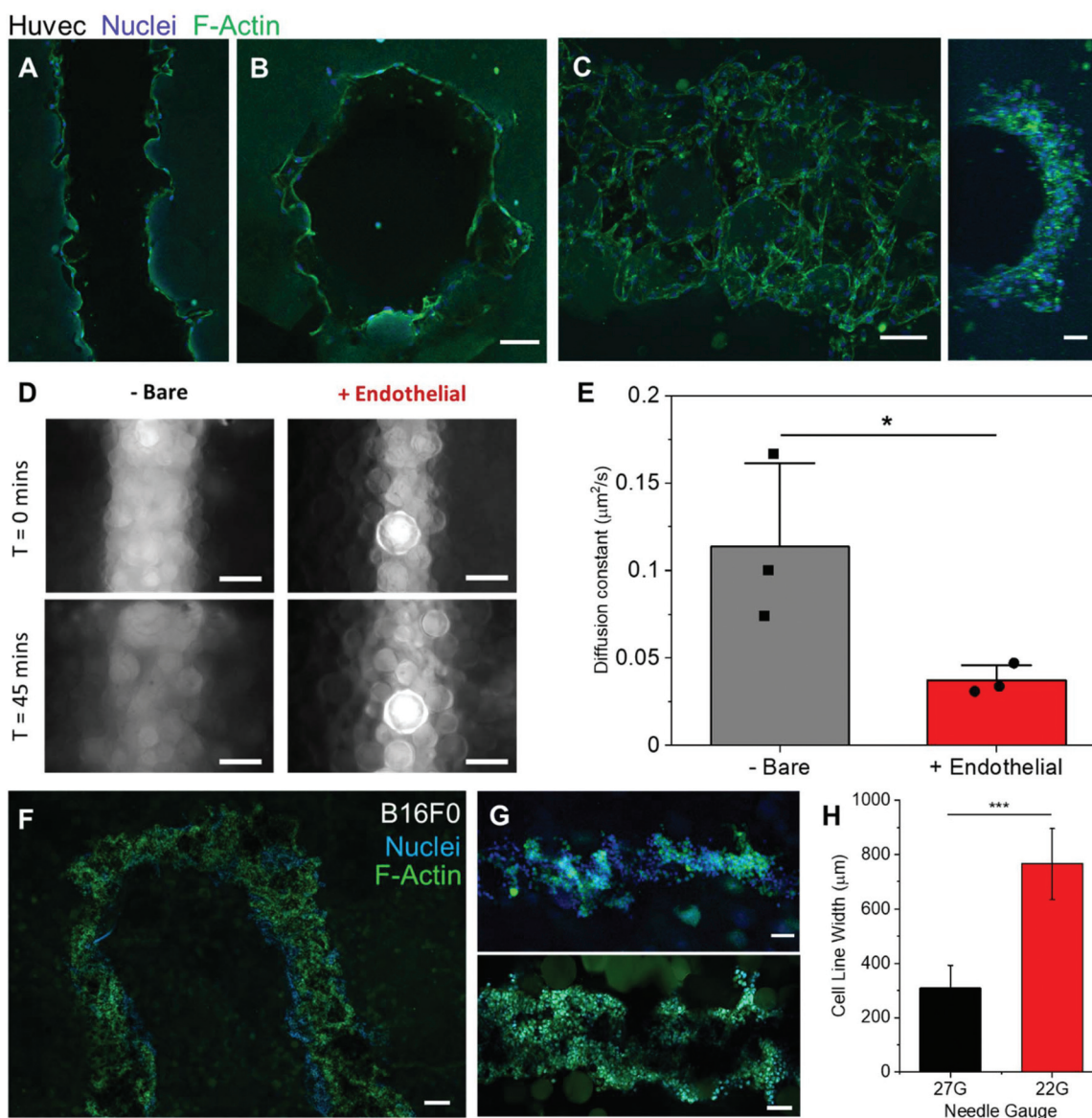
Fig. 4 Vascular cell seeding and cancer cell printing. (A) Confocal plane of Huvec cells seeded along the walls of a printed channel after 5 days. (B) A cross section confocal image of the same gel to verify endothelial cells along the entire channel circumference. (C) A max intensity z-stack projection (left, ImageJ) of the top half of a channel of endothelial cells after 5 days (Huvecs) along with a 3D projection image of the side view of that channel (right). (D) Epifluorescence images taken of 40 kDa FITC-Dextrans in cell-free (left images) and cell laden (right images) vascular channels at the times of 0 (top) and 45 minutes (bottom). (E) Plot of calculated diffusion coefficients of 40 kDa Dextrans in cell laden and cell free vasculature channels ($n = 3$, $p < 0.05$). (F) Confocal image of the top (z-plane) of a U print of a fluidized cell pellet (B16F0). (G) Confocal images of printed tumor lines (B16F0) from a 27G needle (top) and 22G needle (bottom). (H) Plot of the measured average width of tumor line prints from 22G and 27G needles ($n = 6$, $p < 0.001$). Scale bars: 100 μm (A, B, C and G), 200 μm (D and F).

attempted with 0% filler gels to measure if there is variation in endothelial lining tightness and barrier function, however it was not possible to seed the endothelial cells as the gels were too porous. This caused cells to instantly flow throughout the gel when pipetted inside, as well as to be flushed out when external media was applied on top of the gels.

At this stage, we can define blood vessel-like structures within a microgel matrix containing dispersed stromal cells. To investigate the propensity for including tumor-like struc-

tures, a B16 mouse melanoma tumor model was selected due to its high invasiveness and characteristic black color from melanin production which aids with visualization.[33] A cell pellet fluidized with a 3 : 5 ratio of culture medium to cells was chosen as the cell ink for simplicity and a high cell density for *in situ* spheroid production. Parallel lines of printed tumor tissue were first fabricated for viability assessment through live/dead imaging (Fig. S10†). The cell ink was readily extruded and maintained its form while printing with little leakage into

the void space between microparticles (Fig. 4D). Cancer cell line thicknesses can be readily controlled by varying the diameter of the nozzle tip used (Fig. 4G and H). For further modularity, complex shapes can be printed as well as fused together such as rings and thick discs of tumor (Fig. S11†).

2.4 Cancer cell migration through gels and towards vasculature

To explore the role of the matrix on the tumor mimics growth and migration, human melanoma cells (WM266-4, 100 million cells per ml) were printed into granular gels with 1%, 0.5%, and 0% filler. The volume fraction of particles was varied as

30%, 40% and 50% to maintain similar mechanical properties across the gels (Fig. 2B). Two sets of gels were cultured for 2 or 5 days, while one set was fixed immediately after printing to create a baseline of cell position prior to potential migration. No significant differences were found over the three time points for the 1% filler gels; however, the 0.5% and 0% filler granular gels had roughly a ~100% increase and ~150% increase in tumor radius from days 0 to 2 and 5 ($P < 0.0001$), respectively (Fig. 5A). These trends were also verified when printed with a low cell density, demonstrating the initial cell packing plays less of a role than matrix porosity (Fig. S13†). In gels with 0.5% or less filler, there is little hydrogel impeding
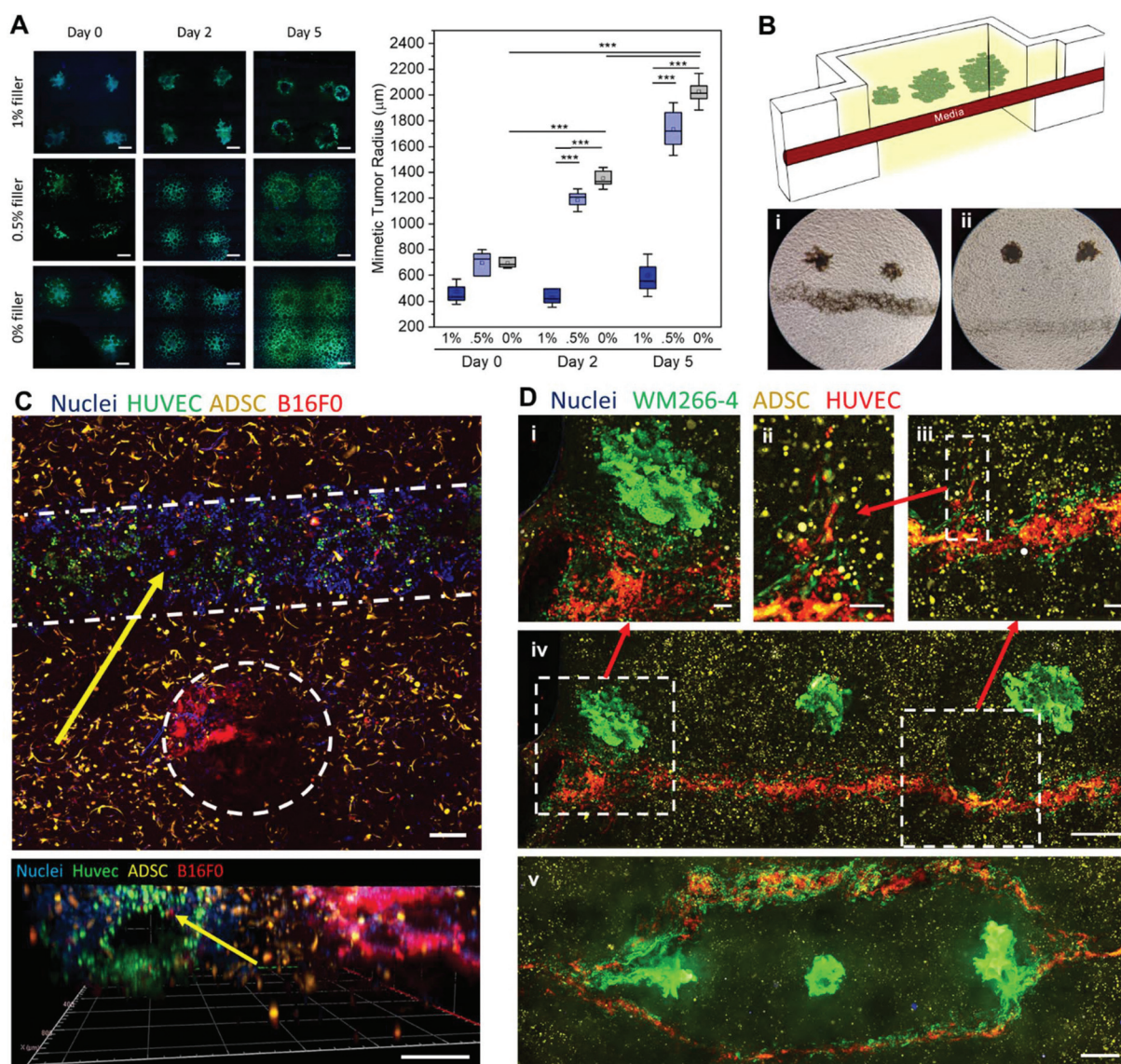

Fig. 5 Printed cancer cell properties and triculture metastasis models. (A) Confocal images of WM266-4 cancer cells printed into granular gels with 3 varied filler percentages at times points of 0, 2, and 5 days. Mimetic tumor radii were quantified at each time point and plot ($n = 5$–12, $p < 0.0001$). (B) A schematic of the tumor invasion model and phase contrast images of tumors printed close (i) and far (ii) from the vasculature. (C) Confocal Z-projection of a triculture of ADSCs, Huvecs in a channel, and printed B16F0 cell pellets (top) along with a 3D projection (Zen blue, Zeiss) of that same gel (bottom). (D) Printed WM266-4 melanoma cells near straight (iv) and bifurcated (v) endothelial lined vasculatures. (i) Represents a zoom in of cell migration from tumor to vasculature while (ii and iii) represent two successive zoom ins of endothelial angiogenesis. Scale bars: 100 μm (D (i, ii and iii)), 200 μm (C), 400 μm (A), 500 μm (D (iv and v)).

the mass migration of cancer cells as they spread and proliferate across and betwen particles. However, the gels with 1% filler have enough matrix for the tumor mimic to degrade that they maintain as a homogenous tumor mass unless given external cues. Therefore, for all further studies, we used 1% filler gels to approximate a more physiologically relevant tumor model.

As a proof of concept to demonstrate a heterotypic tumor microenvironment, we combined tumor printing with vascular printing as a potential model of invasion. We began with printing B16 melanoma aggregates at distances of either 1 mm or 3 mm from the vascular channel (Fig. 5B). Strikingly, before tumor-mediated angiogenesis begins, the cancer cells within 1 mm distance invaded the vasculature in under 4 days, while the tumor aggregates at 3 mm distance did not (Fig. 5B(i and ii)). As paracrine signals play an important role in facilitating cancer cell migration and invasion,[34] we hypothesize that these tumor aggregates may be too far from the vascular lining to perceive endothelial cell-derived signals. As further demonstration of modularity, a triculture model was created by performing both vascular printing and tumor printing simultaneously in a microgel bath laden with adipose derived stromal cells dispersed uniformly throughout the matrix. Here, all three cell types can be seen segregated into their desired locations (Fig. 5C). After five days, tumor cells labelled with CellTracker can be seen intravasating from the tumor mass into the vasculature (Fig. 5C, yellow arrows; Fig. S14†). To verify the phenomenon of directed migration of tumor cells to the vasculature, we extended the tri-culture model to the human WM266-4 melanoma cells (Fig. 5D(i–iv)). Cancer cells were deposited at distances of 0.5, 0.75 and 1.0 mm from the channel center (right to left, Fig. 5D(iv)). A mass migration of tumor cells can be seen in the tumor printed closest to the channel (Fig. 5D(i)) which then invaded throughout the rest of the channel during the 5 days of culture. In contrast, the tumor furthest away induced directional neovascularization from the channel suggesting bi-directional signaling between the two cell types (Fig. 5D(ii and iii)). As a demonstration of versatility, melanoma cells were printed within a hierarchical vasculature (Right and left tumors: distance of 0.5 mm from the bifurcations; Center tumor: 1 mm from the daughter vessels) where extensive migration of tumor cells can be seen at the bifurcations (Fig. 5D(v)).

3 Discussion

The advent of freeform bioprinting has led to a rapid development in tools to reconstruct tissue-like structures for model development and tissue engineering applications.[13,15] Recent work by Feinberg and colleagues and Angelini and colleagues has provided new avenues for bioprinting that obviated the need for overly viscous inks through the use of yield stress fluid support baths, enabling 3D printing of intricate structures with broad flexibility in materials selection.[14,16,19] The two main suspension bath materials used with this printing

technique include Carbopol and gelatin microspheres. While these suspensions have excellent yield stress fluid characteristics that allow for ease of printing, they are typically removed post print.

Rather than using the microgel suspension as a sacrificial printing medium, here we recognized the jammed suspension as a spatially addressable extracellular matrix, in which cellular activity may be dictated by the properties of the suspension. The Segura group and others have explored these types of granular gels as a cell seeded scaffold to capture the benefits the porous nature of the scaffolds provides,[35–37] thereby demonstrating the potential for cells to be integrated with microgels. Recently, Patrício *et al.* showed freeform printing of a sacrificial ink into a alginate microgel bath.[38] And in an interesting twist to the composition of the yield stress fluid for printing, Lewis and colleagues demonstrated freeform vascular printing in a suspension of pure cell organoids.[24] In contrast, while these studies focus on the goal of vascularizing large tissue constructs for regenerative medicine, as does an overwhelming majority of current suspension bath printing studies, our aim was to translate the unique benefits afforded by this spatial control towards establishing *in vitro* models with potential for high throughput assays.[39] We leveraged the benefits associated with the microporous nature of the granular bath to create a cell-laden tunable bioactive matrix, where multiple cell types can be spatially integrated. By coupling a photocrosslinkable filler polymer between the individual microgels, we can stabilize the gels post print enabling removal of a sacrificial ink, unveiling complex channels within the cell-laden matrix. These channels were further modified with endothelial cells towards well defined prototype vessels.

A major advantage with printing in granular media is the ability to print very low viscosity inks without the need for an ink drop printer. Alsberg and colleagues demonstrated this by printing pure pellets of stem cells into their alginate particle baths.[17] In a similar way, we printed tumor aggregates of varied shapes and sizes. Importantly, our approach allows cellular aggregates to be spatially defined in the presence of uniformly dispersed cells and interspersed vascular channels. We demonstrated this by printing microtumors of melanoma cells at varying distances from prototype vessels with evidence for distance-invasion relationships. Microfluidic systems with adjacent chambers and counterflow arrangements have served as complex heterotypic models to monitor signaling between multiple cell types.[40] However, these platforms invariably involve cells adherent to 2D surfaces which disallows variation in the biochemical and biophysical properties of the microenvironment. Our printing system allows similar associations to be fabricated and monitored in a single bioreactor, in a 3D context with tailorable chemistry and mechanics, thereby providing a more biomimetic environment to study cellular processes.

A growing variety of materials have now been used as granular gels for supporting freeform 3D printing, including, but not limited to, pure gelatin, alginate, hyaluronic acid, and Carbopol.[13,15,38,41] While these support gels enable the depo-

sition of compatible hydrogel inks, there are a few key criteria required for the incorporation of vasculature and cells. One, the gel needs binding domains for the cells; two, the gel must be stabilized post print; and three, the support gel must have a mesh size small enough to enable endothelial cells to bind to each other and form tight linings. In our case, we found that without the filler polymer, our mesh size was so large that cells immediately leaked throughout the entirety of the gel. Furthermore, when adding culture medium to surround the gel, the porosity allowed the media to quickly penetrate the network and flush the cells out before they had a chance to adhere to the channel walls. This limitation can be avoided by making granular gels with microparticles smaller than the cells used. However, jammed microgels of small size tend to yield poor cell viability, growth, and fucntion.[19,42] By combining our large microspheres with a dilute filler around them, we maintain the ability to create endothelial linings while still retaining optimal cell conditions in the surrounding gel. The filler polymer also helps prevent unwanted migration from the printed cancer cells. With a sufficiently high enough filler content, the cells maintain more cell–cell connections, staying more as a tumor aggregate, rather than dissociating and spreading throughout the material. Once given some external cue, in our case from endothelial cells, the tumor cells can preferentially dissociate towards the signal, providing scope for the development of tumor models where more sophisticated questions in the biology of metastasis may be investigated.

4 Conclusion

In conclusion, we have demonstrated a bioprinting approach based on a suspension of live cells and crosslinkable granular media, where freeform printing of vascular channels and cellular aggregates is accomplished in a single chamber. Key to this approach is the use of photo-crosslinkable biopolymers to make up the microgels, a filler phase to "stitch" microgels together, and a thermoresponsive Pluronic ink as a sacrificial material to make up the channel. Inspired by the tumor microenvironment, we demonstrate the versatility of this system by integrating prototype tumors and vasculature amidst a matrix of stromal cells. In this way complex processes like tumor intravasation and extravasation, and accompanying roles of stroma-cancer cell interaction, can be readily modelled. Coupled with the ability to simultaneously deposit additional cells with a high degree of spatial control, virtually any number of cell types may be integrated. This new 3D coculture method may provide a means to investigate not only cancer and disease modeling but understanding the role of the extracellular matrix on other cellular processes including tissue morphogenesis in development and disease. Moreover, the high throughput nature of 3D printing combined with this modular approach will allow for combinatorial drug studies to be performed in well-defined models.

5 Materials and methods

5.1 GelMa synthesis

GelMa was synthesized as previously described.[27,43] Briefly, gelatin from porcine skin, Type A (Bloom strength 300, Sigma-Aldrich) was dissolved at 10% (w/v) in 1× phosphate buffered saline (PBS, pH 7.4) under stirring at 50 °C. 5% (v/w) methacrylic anhydride (Sigma-Aldrich) was added and the mixture stirred for 90 minutes. The solution was diluted two-fold with 1× PBS and centrifuged (3000 rcf, 3 minutes) to remove unreacted methacrylic anhydride particulates. Following this, it was transferred into 14 kDa cutoff cellulose dialysis tubes and dialyzed at 40 °C for 5–7 days against deionized water. The dialyzed solution was lyophilized for 5–7 days and the resulting powder stored was stored at −20 °C.

5.2 GelMa microparticle synthesis

The GelMa microparticles were prepared using a modified water in oil emulsion method.[44] The lyophilized GelMa was hydrated to a 10% (w/v) volume solution in 1× PBS at 40 °C. The solution was added dropwise through a 0.45 µm sterile filter into a continuously stirring bath of oil (Canola, Sunflower, Olive) (Community Co., IGA Australia; Bertolli) at 40 °C and allowed to equilibrate for 10 minutes. The bath was cooled to 10 °C for 30 minutes prior to adding acetone (22 mL mL^{-1} GelMa) to dehydrate the microparticles. The particles were then allowed to settle to the bottom of the vessel, washed thoroughly with acetone, and sonicated to break up aggregates. Unbroken aggregates were removed by filtration. The dehydrated microparticles were stored in acetone until use. For size characterization, particles were rehydrated in DI water for one day before taking images on a phase contrast microscope. 100 particles were imaged, and their diameters were calculated using ImageJ.

To prepare the microparticles for printing, acetone was removed by evaporation. The microparticles were hydrated for at least 24 hours in a 1% (w/v) solution of GelMa and 0.05 wt% Lithium phenyl-2,4,6-trimethylbenzoylphosphinate (LAP Sigma-Aldrich, 900889) in either PBS, or appropriate cell culture medium, to achieve a packing fraction of 30% and a final concentration of 1 wt% GelMa in the filler phase as these were determined to be optimal conditions for printing.

5.3 Swelling study

A 10 wt% solution of pure GelMa dissolved in 1× PBS was warmed in an incubator at 37 °C until fully melted. The gel solution (80 µL) was subsequently added to 6 × 6 × 2.5 mm plastic PLA molds and left at room temp to physically crosslink. Once crosslinked, the gels were weighed and placed into 15 mL falcon tubes where they were covered with Acetone (10 mL, Chem-supply) and left to shake for 24 hours. The acetone was then decanted, and the gels were air dried for 24 hours to remove all remaining acetone. The dried gels were then weighed before placing into tubes filled with DI water at room temperature. At each time point, the gels were taken from the tube and the surface water was removed with a

Kimwipe prior to weighing. The swelling ratio was calculated using the following where W is the weight:

$$\text{Swell ratio} = \frac{W_{\text{swelled}} - W_{\text{dried}}}{W_{\text{dried}}}$$

5.4 Rheology

All rheological measurements were performed on an Anton Paar MCR 302 Rheometer with a parallel plate geometry (25 mm Disk, 1 mm measuring distance, 600 µL of suspension bath or Pluronic gel). Oscillatory measurements were performed with 0.02% strain and a 1 Hz frequency for the duration of gelation at 20 °C. For *in situ* UV crosslinking for the GelMa baths, a UV light (with 395 nm UV light at 40 mW cm^{-2} for 60 seconds) was placed underneath to illuminate the sample through the quartz crystal stage. Shear rate sweeps were performed with a 1 Hz frequency from a 0.01 to 10 shear rate (1 s^{-1}) at a log ramp scale over 4 minutes. Temperature stability studies for GelMa baths were run with a temperature ramp from 20 °C to 37 °C. For the melted samples test, the gels were first placed in an incubator at 37 °C for one hour before placing on the rheometer and cooling down to 20 °C before running the test. Strain sweep test were performed with a log ramp up rate from 0.02% shear strain up to 200% at 1 Hz frequency over 8 minutes. For the Pluronic temperature sweep, the samples were cooled down in the fridge to 4 °C before placing them on the rheometer at 1 °C. The temperature was ramped up from 1 °C to 37 °C at a rate of 1 °C per minute with a 0.02% shear strain at 1 Hz frequency. The frequency sweep was run with a log ramp up rate from 0.01 to 100 Hz with a 0.02% strain.

5.5 Atomic force microscopy (AFM)

Suspensions of $30V_f$ GelMa particles with filler were crosslinked in 6 × 6 × 1 mm plastic molds glued down to glass coverslips. Shorter molds were used to limit light diffraction for the camera on the AFM's microscope. The samples were fixed to the bottom of fluorodishes (Coherent, FD35) with 2-part rubber cement. The samples were then submerged in water until ready. All data was acquired with the JPK NanoWizard4 Bio-AFM with a spherical probe (2 µm diameter Borosilicate unmodified probe, Novascan). The tip spring constant was calibrated on glass in water prior to the experiment. Using contact-force micropy mode, 36 force curves (6 µm approach at 0.5 µm per second) were taken per 10 × 10 µm regions in different locations of the gel. A stitched optical image was taken to find particles and filler spaces between. The curves were loaded in the JPK Data Processing software to calculate the elastic modulus at each region. The following analysis steps were performed:

1. Gaussian smoothing of the curve with a smoothing width of 3.00.

2. Baseline subtraction with tilt using the last 40% of the curve along the *x*-axis.

3. Automatic contact point adjustment.

4. Vertical tip position calibration using the unsmoothed height.

5. An elasticity fit using the Hertz/Sneddon model with a spherical tip shape with a 1 µm tip radius and 0.50 Poisson ratio.

5.6 Cell culture and seeding in bulk suspensions

The B16F0 (ATCC) cells were cultured with high glucose Dulbecco's Modified Eagle Medium (DMEM) supplemented with 10% FBS and 1% Penicillin/Streptomycin. Adipose derived stem cells (ADSCs, PSC-500-011 ATCC) were cultured in low glucose DMEM supplemented with 10% FBS and 1% Penicillin/Streptomycin. GFP-WM266-4 cells with were cultured in Minimum Essential Medium Eagle (MEME) with 10% FBS, 1% Glutamax, and 1% Penicillin/Streptomycin. HUVECs (Lonza C2519A) were cultured with the Endothelial Cell Growth Medium-2 BulletKit (Lonza CC-3162) All cultures were maintained at 37 °C, 5% CO_2 and used between passages 2–13. For ADSCs seeding in the hydrogel matrices, the cells were detached with trypsin, counted, centrifuged down, and resuspended to 2×10^7 cells per mL. The cells were then added in a 1 : 20 volume ratio to either a solution of 10 wt% GelMa at 37 °C or a prehydrated bath of GelMa particles at room temperature for a final concentration of one million cells per mL. In order to intermix the cells with the granular gels, the solutions were pipetted up and down extensively before centrifugation at 300 rcf for 3 minutes to remove air bubbles that had been added. These solutions were subsequently supplemented to 0.05 wt% LAP with a 2.5 wt% stock. 80 µL of each gel solution was then added to plastic printed molds (6 × 6 × 2.5 mm) where they were crosslinked under a 395 nm light torch (eBay; 100 LED 395 nm UV Ultraviolet Flashlight Blacklight Torch) at 40 mW cm^{-2} for 60 seconds. The cells were added to a 24 well plate with 1 ml of media. Media was changed after one day followed by every other day. The gels were cultured for 1–7 days before fixation with PFA.

5.7 Cell viability analysis

For ADSCs, 1 million cells per mL were loaded into both the 10 wt% GelMa solution and 30-volume fraction microgel bath, each with 0.05 wt% LAP. Next, 80 µL of gel was placed into a 6 × 6 × 2.5 mm plastic mold where the gels were crosslinked for 1 minute. For the B16F0s, the cell ink was prepped as specified elsewhere. Three lines (22G needle, 5 mm long) of cancer cells were printed into each gel prior to crosslinking. All cell loaded gels were placed into a 24 well plate and cultured for the specified time. Media changes were made on days 1, 3, and 5. For the staining, the media was removed and the gels were washed once with PBS prior to the addition of 500 µL of 1× PBS with Calcein AM (2 µM) and Ethidium Homodimer-1(4 µM) (Invitrogen, L3224). After 45 minutes of incubating the stains, the gels were rinsed with PBS and washed again with PBS after 10 minutes before imaging on a Zeiss LSM 800 Confocal microscope.

5.8 Immunofluorescence staining and tissue clearing

Clearing solutions were prepared as done previously with minor modifications (Molley 2020, susaki 2014). Briefly, Cubic solution 1 was prepared by mixing 25 wt% urea (Sigma Aldrich., 583051), 25 wt% N,N,N′,N′-tetrakis(2-hydroxypropyl) ethylenediamine (Sigma Aldrich, 585714), and 5 wt% Triton X-100 (Sigma Aldrich, 562380) into DI water at 50 °C until fully dissolved. Cubic solution 2 was prepared by mixing 50 wt% sucrose (Sigma Aldrich, 584173), 25 wt% urea, 10 wt% tri-ethanolamine (Sigma Aldrich, 90278–100 mL) with DI water at 55 °C until also fully dissolved. Microgel suspensions were fixed using a 4 wt% paraformaldehyde (Chem-Supply) for 1–4 days at room temperature to ensure fully penetration of PFA into thick constructs. The gels were then rinsed with PBS followed by 3 PBS washes at 2–4-hour intervals. The Hoechst (1 : 1000) and 488-Phalloidin (1 : 200) staining was then performed overnight at room temperature. The gels were washed with PBS three final times before the addition of the Cubic 2 clearing solution for 2–5 days. All confocal imaging was performed with a Zeiss LSM 800. A 10× objective with a 2.5 mm working distance was used to see deeper into the samples. Samples were coated with clearing 2 solution throughout the duration for the imaging to prevent drying.

5.9 Cell volume segmentation analysis

For cell volume analysis, one million ADSCs were loaded into microgel suspensions and bulk hydrogels before crosslinking for 60 seconds. At the desired time points, the cells were fixed with 4% PFA for 24 hours before staining (Hoechst, 405; Phalloidin, 488) and cleared as mentioned above. Confocal z-stacks (20× objective, 109 slices over 50 μm) were taken of representative regions in each gel. The images were imported in Imaris 9.5.1 for analysis. Cell segmentations were created using the Cell module with the phalloidin stain as the cell body and Hoechst for the cell nuclei. For each image was analyzed using identical thresholding values per gel with each independent nucleus as a seed for the cells.

5.10 Plastic reactor mold fabrication

All plastic reactor molds were 3D printed with a Lulzbot Mini2 plastic 3D printer with a 0.25 mm nozzle end. For cell experiments, molds are fixed to an 18 mm diameter glass coverslip with cyanoacrylate glue. The molds are then quickly soaked with 80 vol% ethanol and dried out inside of a biosafety cabinet prior to use. For non-cell experiments, the reactors are pressed into stretched parafilm before addition of the microgel suspension and subsequent crosslinking. STL files for the molds can be found here: https://www.thingiverse.com/tmolley/collections/freeform-vascular-printing-designs.

5.11 Pluronic ink preparation

To create the sacrificial inks, Pluronic F127 (Sigma, P2443-250G) was first weighed out into 50 mL flacon tubes. Cold DI water (4 °C) was then added to the Pluronic powder for the appropriate weight percentage. The mixture was mechanically agitated before placing into a fridge at 4 °C overnight to fully dissolve the ink. The ink was then stored at 4 °C until further use.

5.12 MicroCT and volume segmentation

MicroCT scan was performed with the U-CT (MILabs, Utrech), with 50 kVp X-ray tube voltage, 0.21 mA tube current, 75 ms per frame, 360° angle, and 0.25° projections. Images were reconstructed with MILabs Recon 10.16 at 20 μm voxel size and vessels segmented using Imalytics Preclinical 2.1 (Gremse-IT GmbH, Germany).

5.13 CFD and analysis

Computational fluid dynamics (CFD) analysis was run with the Autodesk CFD 2019® software. The segmented STL meshes exported from Imalytics Preclinical 2.1 were imported in Autodesk 360 Fusion® to reduce the mesh network down to <10 000 polygons for smoother modeling. Theoretical model designs were created in Autodesk Inventor CAD to represent the shape the gcode was supposed to create. The mesh volumes were the loaded in the CFD software and the following assumptions were made:

1. Volume is specified as water.
2. End boundary condition set to 0 Pa pressure.
3. Automatic meshing.
4. 0 initial conditions.
5. Fluid is incompressible.
6. Flow was set to a kappa-epsilon turbulent flow model with a turbulent : lamilar flow ratio of 100 : 1.
7. ADV 5 modified Petrov–Galerkin advection.
8. 100 iterations were performed with a steady state solution mode.
9. Flow rate defined as 150 nL s^{-1} for the straight channel and 300 nL s^{-1} for the bifurcation.
10. The bifurcation had flow originating from the single channel end.

Videos of flow traces were recorded and exported from the software.

5.14 Printing (vasculature, tumors, co-culture cell baths)

5.14.1 Printing vasculature. A Lulzbot mini2 retrofitted with a screw extrusion syringe head (Replistruder head 2, Feinberg lab) was placed into a Biosafety cabinet. For Pluronic printing, the 29 wt% Pluronic F127 solution was cooled down in a fridge (4 °C), then pulled into an airtight glass syringe (Hamilton® 1002LTN syringe) and inverted to remove air bubbles. The syringe was warmed to room temperature to gel the Pluronic F127 before loading into the printer. A 22G Nordson EFD needle tip was added to the syringe and a small amount of Pluronic was extruded out to prime the needle tip. The print needle was then orientated over and aligned with the inlet and the suspension was added to the mold until the surface of the liquid was flush with the top of the mold. The desired print code was run, and the needle was gently cleaned with a Kimwipe prior to the next print. The suspension was then photocrosslinked for 1 minute, placed into a 12 well

plate, parafilmed, and put in a fridge for 15 minutes to liquify the Pluronic F127. For print fidelity measurements, the ink was removed and Phase contrast images of the air inside the channel were taken. Analysis was performed *via* ImageJ along 6 diameters for each line to determine the lines average thickness.

5.14.2 Direct printing of cells. The desired cells were treated with trypsin, centrifuged, washed, and then pelleted. The cell pellets were lightly fluidized with media in a 5 : 3–5 : 2 ratio of cells to media to break up aggregates. Care was taken to limit the introduction of air bubbles during this stage. The pellet was then pulled into a 1 mL syringe (Livingston), and the syringe was loaded directly into a 3D printed fitting on the bioprinter. The desired syringe needle was then primed with cell solution and printed into molds filled with a microgel suspension.

5.14.3 Dual cell and vascular printing. Each part of the multistage printing process was performed as mention above with some modifications. Importantly, cell printing preceded vascular printing as the Pluronic ink begins to diffuse into the surrounding suspension if not crosslinked fast enough leading to poor channel resolution. In addition, after cell printing, the molds are placed into a covered, sterile Petri dish to enable easy access while limiting overhead airflow that can dry out or contaminate the microgel suspension.

5.14.4 Incorporating cells into suspensions. When incorporating cells into the support suspensions, the microparticles were first hydrated with the appropriate culture medium. The cells were treated with trypsin, centrifuged to a pellet, then resuspended to a 50× cells mL concentration compared to the final volume. The high concentration cell solution was gently mixed into the hydrated microparticles before adding to the molds. Printing was then conducted as mentioned prior.

5.15 Loading vascular cells in printed vasculature and subsequent co-culture

The microgels were placed into a fridge for 15 minutes to allow the Pluronic F127 to transition into a liquid state. It was then removed *via* holes at either end of the mold, leaving behind a hollow channel. Endothelial cells (HUVECs at 10–20 million cells per mL) were loaded into a 1 mL syringe and injected into the channel through the same holes at either end of the mold. The microgel was inverted and placed in a 12-well plate, then placed in the incubator for 30 minutes. The vessels were then flipped back upright and incubated for another 30 minutes before adding the cell media. The construct was cultured at 37 °C for 4–7 days.

5.16 Fidelity of tumor prints

For tumor line prints, a sacrificial print was first made above the microgel suspension to prime the needle tip. Once printed, the microgels were immediately fixed with 4% PFA. After fixation and washing of the fixed microgels, they were added to a 5 wt% solution of Hydrogen Peroxide (Sigma Aldrich, 487568) at room temperature for 24 hours to bleach the melanin and aid in confocal imaging. The samples were then stained with Hoechst and Phalloidin and z-stack tile scans of the gels were taken. Analysis was performed in ImageJ. First, the z-stacks were projected into one slice with using the maximum brightness. The images were then thresholded in the phalloidin channel to outline the lines, followed by 6 length measurements taken across the length of the tumor lines.

5.17 Endothelial barrier function

Printed channels were formed in 1% filler granular gels and either loaded with endothelial cells or 1× PBS. After 4 days, the gel channels, with live cells, were loaded with 40 kDa FITC-dextran (100 µg mL^{-1}, Sigma FD40-100MG) before placing on a wide-field fluorescent microscope. Images were taken of the channels every 5 minutes for 45 minutes and imported into MATLAB for analysis. We assume that the fluorescent intensity of the FITC dextran is directly proportional to the dye concentration. And we also assume that the dye undergoes 1D fickian diffusion. Using this, we fit middle profile of each image is fitting to a Gaussian function for each time point to obtain the spatial peak variance fitting parameter σ^2. By using the Einstein–Smoluchowski relation:

$$\sigma^2 = 2Dt$$

where σ^2 is the spatial peak variance, D is the diffusion constant, and t is time, we can plot σ^2 as a function of time to determine the diffusion constant.

5.18 NMR for GelMa methacrylation characterization

The degree of functionalization (DOF) was quantified using a ^{1}H NMR spectrometer (Bruker Avance III 400 MHz) by referencing ^{1}H NMR chemical shifts to the residual solvent peak at 4.80 ppm in D$_2$O. Briefly, 10 mg of GelMA was dissolved in 1 mL of D$_2$O at 37 °C. 700 µL was put into an NMR tube for the acquisition of the NMR data. NMR spectra were analyzed using MestReNova (Mestrelab Research) by Dr Julio Serrano (University of Illinois at Urbana-Champaign), using the chemical shift in the aromatic region as integral reference. Degree of functionalization of 96 and 98% can be seen in Fig. S15.† ^{1}H NMR (400 MHz, D$_2$O): δ 7.24 (m), 5.65 (m), 5.40 (m).

5.19 Statistical analysis

The whiskers in the box plots are standard deviation (s.d.) unless otherwise specified. Analyses of tumor migration radii were calculated in imageJ. Statistical significance was determined using a one-way ANOVA with Tukey's Post Hoc HSD analysis. Differences were considered significant when $P < 0.05$.

Conflicts of interest

There are no conflicts of interest to declare.

Acknowledgements

References

1 A. Malandrino, R. D. Kamm and E. Moeendarbary, *ACS Biomater. Sci. Eng.*, 2018, **4**, 294.

2 M. Nicolau, A. J. Levine and G. Carlsson, *Proc. Natl. Acad. Sci. U. S. A.*, 2011, **108**, 7265.

3 C. E. Tschirhart, A. Nagpurkar and C. M. Whyne, *J. Biomech.*, 2004, **37**, 653.

4 J. M. Bailey, A. M. Mohr and M. A. Hollingsworth, *Oncogene*, 2009, **28**, 3513.

5 M. C. Kwon, N. Proost, J. Y. Song, K. D. Sutherland, J. Zevenhoven and A. Berns, *Genes Dev.*, 2015, **29**, 1587.

6 Y. Chen, X. Gou, D. K. Kong, X. Wang, J. Wang, Z. Chen, C. Huang and J. Zhou, *Oncotarget*, 2015, **6**, 32575.

7 I. J. Fidler, S. Yano, R. D. Zhang, T. Fujimaki and C. D. Bucana, *The seed and soil hypothesis: Vascularisation and brain metastases*, Lancet Publishing Group, 2002.

8 S. Kenig, M. B. D. Alonso, M. M. Mueller and T. T. Lah, *Cancer Lett.*, 2010, **289**, 53.

9 S. Rao, R. Sengupta, E. J. Choe, B. M. Woerner, E. Jackson, T. Sun, J. Leonard, D. Piwnica-Worms and J. B. Rubin, *PLoS One*, 2012, 7, e33005.

10 M. Upreti, A. Jamshidi-Parsian, N. A. Koonce, J. S. Webber, S. K. Sharma, A. A. A. Asea, M. J. Mader and R. J. Griffin, *Transl. Oncol.*, 2011, **4**, 365.

11 C. Wang, J. Li, S. Sinha, A. Peterson, G. A. Grant and F. Yang, *Biomaterials*, 2019, **202**, 35.

12 Y. Kam, K. A. Rejniak and A. R. A. Anderson, *J. Cell. Physiol.*, 2012, **227**, 431.

13 T. Bhattacharjee, S. M. Zehnder, K. G. Rowe, S. Jain, R. M. Nixon, W. G. Sawyer and T. E. Angelini, *Sci. Adv.*, 2015, **1**, e1500655.

14 C. D. Morley, J. Tordoff, C. S. O'Bryan, R. Weiss and T. E. Angelini, *Soft Matter*, 2020, **16**, 6572.

15 T. J. Hinton, Q. Jallerat, R. N. Palchesko, J. H. Park, M. S. Grodzicki, H.-J. Shue, M. H. Ramadan, A. R. Hudson and A. W. Feinberg, *Sci. Adv.*, 2015, **1**, e1500758.

16 A. Lee, A. R. Hudson, D. J. Shiwarski, J. W. Tashman, T. J. Hinton, S. Yerneni, J. M. Bliley, P. G. Campbell and A. W. Feinberg, *Science*, 2019, **365**, 482.

17 O. Jeon, Y. B. Lee, H. Jeong, S. J. Lee, D. Wells and E. Alsberg, *Mater. Horiz.*, 2019, **6**, 1625–1631.

18 N. Noor, A. Shapira, R. Edri, I. Gal, L. Wertheim and T. Dvir, *Adv. Sci.*, 2019, **6**, 1900344.

19 S. Romanazzo, T. G. Molley, S. Nemec, K. Lin, R. Sheikh, J. J. Gooding, B. Wan, Q. Li, K. A. Kilian and I. Roohani, *Adv. Funct. Mater.*, 2021, 2008216.

20 A. C. Daly, L. Riley, T. Segura and J. A. Burdick, *Hydrogel microparticles for biomedical applications*, Nature Research, 2020.

21 W. Wu, A. Deconinck and J. A. Lewis, *Adv. Mater.*, 2011, **23**, H178.

22 D. B. Kolesky, K. A. Homan, M. A. Skylar-Scott and J. A. Lewis, *Proc. Natl. Acad. Sci. U. S. A.*, 2016, **113**, 3179.

23 K. Kobayashi, Y. Ichihara, N. Sato, N. Umeda, L. Fields, M. Fukumitsu, Y. Tago, T. Ito, S. Kainuma, M. Podaru, F. Lewis-McDougall, K. Yamahara, R. Uppal and K. Suzuki, *Biomaterials*.

24 M. A. Skylar-Scott, S. G. M. Uzel, L. L. Nam, J. H. Ahrens, R. L. Truby, S. Damaraju and J. A. Lewis, *Sci. Adv.*, 2019, **5**, eaaw2459.

25 S. A. Wickström and C. M. Niessen, *Cell adhesion and mechanics as drivers of tissue organization and differentiation: local cues for large scale organization*, Elsevier Ltd, 2018.

26 E. Potier, J. Noailly and K. Ito, *Directing bone marrow-derived stromal cell function with mechanics*, Elsevier, 2010.

27 E. A. Susaki, K. Tainaka, D. Perrin, H. Yukinaga, A. Kuno and H. R. Ueda, *Nat. Protoc.*, 2015, **10**, 1709.

28 T. G. Molley, X. Wang, T. Hung, P. B. Jayathilaka, J.-L. Yang and K. A. Kilian, *Adv. Biosyst.*, 2020, 2000056.

29 N. Y. C. Lin, K. A. Homan, S. S. Robinson, D. B. Kolesky, N. Duarte, A. Moisan and J. A. Lewis, *Proc. Natl. Acad. Sci. U. S. A.*, 2019, 201815208.

30 D. B. Kolesky, R. L. Truby, A. S. Gladman, T. A. Busbee, K. A. Homan and J. A. Lewis, *Adv. Mater.*, 2014, **26**, 3124.

31 J. L. Rein, S. Heja, D. Flores, R. Carrisoza-Gaytán, N. Y. C. Lin, K. A. Homan, J. A. Lewis, L. M. Satlin and L. Nyc, *Am. J. Physiol.: Cell Physiol.*, 2020, **319**, 136.

32 W. J. Polacheck, M. L. Kutys, J. Yang, J. Eyckmans, Y. Wu, H. Vasavada, K. K. Hirschi and C. S. Chen, *Nature*, 2017, **552**, 258.

33 J. Lee, A. A. Abdeen, K. L. Wycislo, T. M. Fan and K. A. Kilian, *Nat. Mater.*, 2016, **15**, 856.

34 Y. H. Wang, Y. Y. Dong, W. M. Wang, X. Y. Xie, Z. M. Wang, R. X. Chen, J. Chen, D. M. Gao, J. F. Cui and Z. G. Ren, *J. Exp. Clin. Cancer Res.*, 2013, **32**, 1.

35 N. F. Truong, E. Kurt, N. Tahmizyan, S. C. Lesher-Pérez, M. Chen, N. J. Darling, W. Xi and T. Segura, *Acta Biomater.*, 2019, **94**, 160.

36 D. R. Griffin, W. M. Weaver, P. O. Scumpia, D. D. Carlo and T. Segura, *Nat. Mater.*, 2015, **14**, 737.

37 A. Kodali, T. C. Lim, D. T. Leong and Y. W. Tong, *Macromol. Biosci.*, 2014, **14**, 1458.

38 S. G. Patrício, L. R. Sousa, T. R. Correia, V. M. Gaspar, L. S. Pires, J. L. Luís, J. M. Oliveira and J. F. Mano, *Biofabrication*.

39 K. H. Song, C. B. Highley, A. Rouff and J. A. Burdick, *Adv. Funct. Mater.*, 2018, 1801331.

40 M. Rothbauer, H. Zirath and P. Ertl, *Recent advances in microfluidic technologies for cell-to-cell interaction studies*, Royal Society of Chemistry, 2018.

41 K. H. Song, C. B. Highley, A. Rouff and J. A. Burdick, *Adv. Funct. Mater.*, 2018, **28**, 1801331.

42 K. Hayashi and Y. Tabata, *Acta Biomater.*, 2011, **7**, 2797.

43 D. Loessner, C. Meinert, E. Kaemmerer, L. C. Martine, K. Yue, P. A. Levett, T. J. Klein, F. P. W. Melchels, A. Khademhosseini and D. W. Hutmacher, *Nat. Protoc.*, 2016, **11**, 727.

44 T. Phromsopha and Y. Baimark, *Int. J. Biomater.*, 2014, **2014**, 829490.